J Braz. Soc. Mech. Sci. Eng. (2017) 39:1375–1390
DOI 10.1007/s40430-016-0584-9

TECHNICAL PAPER

Comparison between elastic properties of theoretical, computational method and experimental results for filament wound composite pipes

A. Ortenzi[1] · **J. Carvalho**[2] · **A. Corvi**[3]

Received: 14 July 2015 / Accepted: 3 June 2016 / Published online: 24 June 2016
© The Brazilian Society of Mechanical Sciences and Engineering 2016

Abstract This work compared the experimental results obtained through tensile tests of epoxy pipes reinforced with glass fibers, produced by filament winding with angular variations of ±50°, ±52.5° and ±55°. The elastic properties of the pipes were calculated for each typology using the rule of mixtures and classical laminate theory. Concurrently, finite element modeling was performed for each angular variation under a load identical to the experimental case. The obtained values were compared according to the angular variation of each typology. Means and standard deviations were calculated and compared. The values obtained in the tests were convergent with the design and finite element approach. It was also found that for small angular variations, the moduli for a given composite constitution changed significantly, as observed in the results. Furthermore is suggested to modify the strain gages position regarding the winding angles to compare with results achieved.

Technical Edotor: Eduardo Alberto Fancello.

✉ A. Ortenzi
ortenzi@sc.usp.br

J. Carvalho
prjonas@sc.usp.br

A. Corvi
andrea.corvi@unifi.it

[1] Civil Engineering Department, Londrina State University, Londrina, Brazil

[2] Mechanical Engineering Department, University of São Paulo, São Paulo, Brazil

[3] Industrial Engineering Department, University of Florence, Florence, Italy

Keywords Composites · Filament winding · FEA · Structural analylis · Pipes

1 Introduction and objectives

This paper describes the validation of an integrated design and simulation approach via the comparison of the results of tensile tests conducted on filament wound pipes prior to the development of the whole research, with other 45 specimens.

The tensile tests revealed that large hoop and helical displacements are caused by exceeding a loading threshold and that the damage behavior varies with the angular variation, temperature, and number of bundles used in the fabrication of these structural elements (Fig. 1a, b).

The first paper in this series covered the preliminary analysis of acoustic emission behavior for the same sample typology [1]. In this work, the correlation between the three winding angles was investigated, and the variation of their elastic properties was used as a control parameter throughout the research project.

The approach developed in this work assumes that the composite structures are formed by assembling their raw materials, which are created individually, rather than treating these structures as homogeneous and isotropic single materials.

2 Literature review

Pipes in composite structures are generally fabricated via filament winding. This industrial process requires control of the roving slippage, angular path variation and inversion, head tension, and rotation of the mandrel throughout the lamination process. In this work, the angular path control is analyzed.

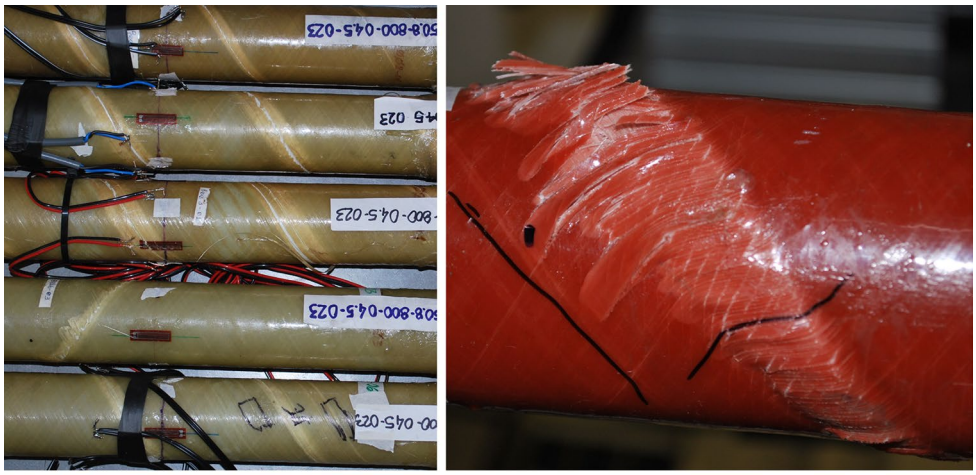

(a) **(b)**

Fig. 1 **a** Set of specimens tested at room temperature. **b** Detail of displacement for specimens tested at 85 °C

Table 1 Density according to the experimental results

Type of specimen	Volume of sample (m^3)	Volume of fiber (m^3)	Weight of sample (kg)	Density of sample (kg/m^3)	Weight of fiber (kg)	Density of fiber (kg/m^3)
±50.0°	7.547E−7	3.957E−7	0.0016	2035.80	0.00104	2620.00
±52.5°	7.834E−7	4.547E−7	0.0016	2050.04	0.00120	
±55.0°	8.039E−7	4.700E−7	0.0017	2055.60	0.00123	

Table 2 Fiber ratio according to the Table 1

Winding angle	W_{fr}	V_{fr}
±50.0°	69.3403	0.54
±52.5°	69.9795	0.55
±55.0°	71.7592	0.56

W_{fr} averaged weight fiber ratio, V_{fr} Averaged volumetric fiber ratio

Table 3 Total number of paths to complete one layer as a function of the mandrel radius

Mandrel radius	Winding angle	Turns	$w = 6$ bundles (mm)
25.40 (mm)	±50°	±5 (± 4.38)	23.4
	±52.5°	±5 (± 4.15)	23.4
	±55°	±4 (± 3.91)	23.4

The calculation models most commonly used in the design of composite structures are classical laminate theory (CLT) and the rule of mixtures (RM), both of which have been discussed extensively in the literature [2–9].

Several published studies have investigated tubular specimens produced by filament winding, which used finite-element software to propose ways to predict the failures in the matrix and in the filaments [10].

Table 4 Elastic properties found through the mRM

Parameter[a]	Winding angle		
	±50.0°	±52.5°	±55.0°
V_{fr}	0.54	0.55	0.56
E_f (GPa)	81.5	81.5	81.5
E_m (GPa)	3.6	3.6	3.6
E_{11} (GPa)	15.11	14.67	14.20
E_{22} (GPa)	37.01	37.28	37.67
G_{12} (GPa)	8.79	8.79	8.79
G^b_{23} (GPa)	2.65	2.68	2.73
ν_f	0.22	0.22	0.22
ν_m	0.4	0.4	0.4
ν_{12}	0.315	0.297	0.271
ν_{21}	0.129	0.117	0.102
S_T (mm^2)	572.535	570.467	560.376
σ_1 (MPa)	6.00	6.02	6.13
σ_2 (MPa)	4.64	4.55	4.42
ε_1 (mm/mm)	0.000397	0.000411	0.000432
ε_2 (mm/mm)	−0.000125	−0.000122	−0.000117

[a] Local coordinates

[b] G_{23} = out of bundle plane shear modulus

Previous works have verified the behavior of pipes manufactured by filament winding. In one study, these pipes, manufactured with a winding angle of ±55°, were

Table 5 Elastic properties found through CLT

Parameter	Winding angle		
	±50.0°	±52.5°	±55.0°
V_{fr}	0.54	0.55	0.56
E_f (GPa)	81.5	81.5	81.5
E_m (GPa)	3.6	3.6	3.6
E_{11} (GPa)	11.69	11.07	10.23
E_{22} (GPa)	37.12	37.30	37.78
G_{12} (GPa)	7.68	7.18	6.50
v_f	0.22	0.22	0.22
v_m	0.4	0.4	0.4
v_{12}	0.424	0.392	0.353
v_{21}	0.134	0.116	0.096
S (mm^2)	572.535	570.467	560.376
σ_1 (MPa)	6.00	6.02	6.13
σ_2 (MPa)	4.64	4.55	4.42
ε_1 (mm/mm)	0.000382	0.000403	0.00043
ε_2 (mm/mm)	−0.000162	−0.000158	−0.000152

subjected to biaxial compression [11]. In another study, several theoretical models were compared with the experimental results obtained for specimens manufactured by filament winding at ±55° and then, subjected to biaxial compression and internal pressure tests [12].

For a more detailed description of the failure analysis criteria, please refer to the relevant studies in the literature [13–19].

Rousseau et al. [20] experimentally verified the effects and occurrences of progressive failure leading to fractures in pipes. The loss of stiffness was verified by comparing the deformed and undeformed geometries. In particular, the geometry of the roving formed a diamond shape in which the filaments intersected the preceding filaments, and this diamond was different in the deformed state. As a result, the successive deformation after each variation of the load level changed. Other studies conducted similar analyses in pipes wound at ±60° and ±45° [21].

The literature also contains studies on the effects of the environment. Aggressive environmental effects were found to cause a loss of adherence between the fiber and matrix in pipes wound at ±60° and subjected to internal pressure at different temperatures [22].

Some researchers have analyzed the shear stresses induced by tensile stress acting on a pipe and the correlation of these stresses with the torsional stress, internal pressure, and circumferential stress in pipes wound at ±45° [23] or the behavior of pipes wound at ±54.7° with different wall thicknesses [24].

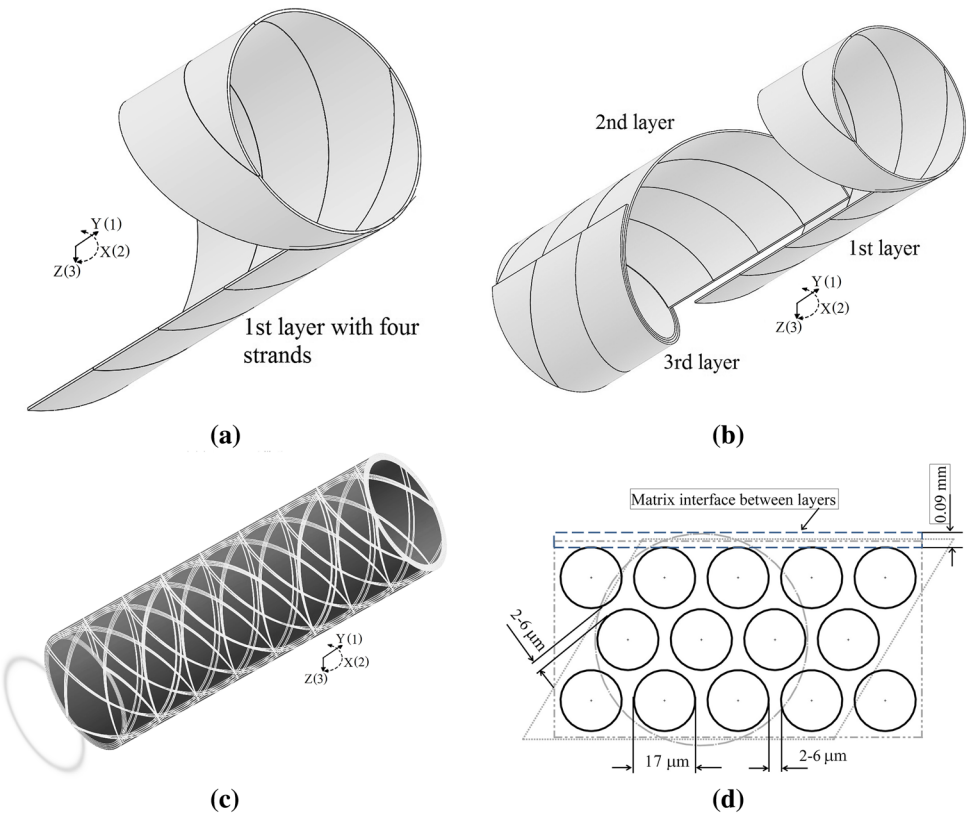

Fig. 2 **a–c** Stacked sequence. **d** Study of possible geometric arrangements of filaments, according to Eq. 2

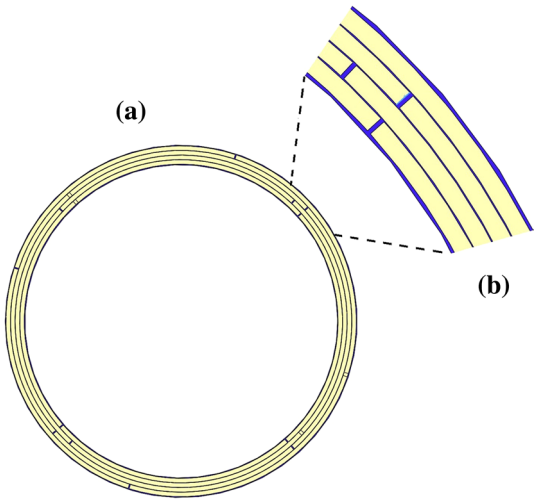

Fig. 3 **a** Cross section of the strands. **b** Detail of strands separation and matrix

Hu et al. [25] conducted a study that is somewhat similar to that presented here. However, they only considered pipes wound at ±55°, and their finite-element analysis (FEA) did not utilize a parametric model that considers the raw materials individually.

Based on this literature review, it is clear that although filament wound pipes have been studied extensively, these studies differ in terms of the raw materials, fiber orientation, or nature of the polymeric matrix considered [26–36].

3 Materials and methods

3.1 Specimens

The specimens were fabricated with three different typologies, winding the pipes at ±50.0°, ±52.5°, and ±55.0°. For each typology, 15 samples were produced with the same geometrical parameters: 300 mm of total length, 180 mm span length, 50.8 mm internal diameter, and 3.2 mm wall thickness.

Three specimens for each winding angle were randomly sampled, and the fiber volume fraction V_{fr} was obtained experimentally based on ASTM D3171 [37] procedure *A* (Tables 1, 2).

Equation 1 was used to calculate the number of layers needed to achieve the target design thickness, which was used as an input in the filament winding process (Table 3).

$$N = \frac{2\pi R_{avg} \tan \alpha}{w} \tag{1}$$

where N = total number of paths to complete the closing equivalent layer of roving, w = band width, $R_{avg} = (D_e - t)/2$, where t = wall thickness and D_e = external diameter of the pipe, α = winding angle.

3.2 Theoretical composite properties

The theoretical analysis was conducted using the well-known modified RM (mRM) and CLT approaches. First,

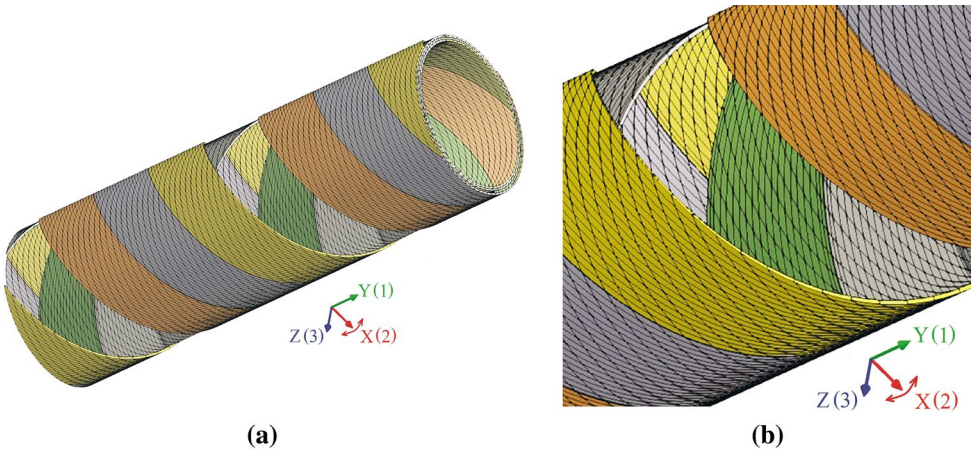

Fig. 4 **a** Hexahedral mesh. **b** Mesh detail

(a) **(b)**

Table 6 Material properties used as the input data for simulation

Material	Temperature (°C)	E_{11} modulus (GPa)	Poisson's ratio	G_{12} modulus (GPa)	G_{23} modulus (GPa)
ECR -Roving	25	81.5	0.22	5.02	3.17
Epoxy	25	3.6	0.4	0.3	0.14
Structural steel	25	210	0.3	141	179

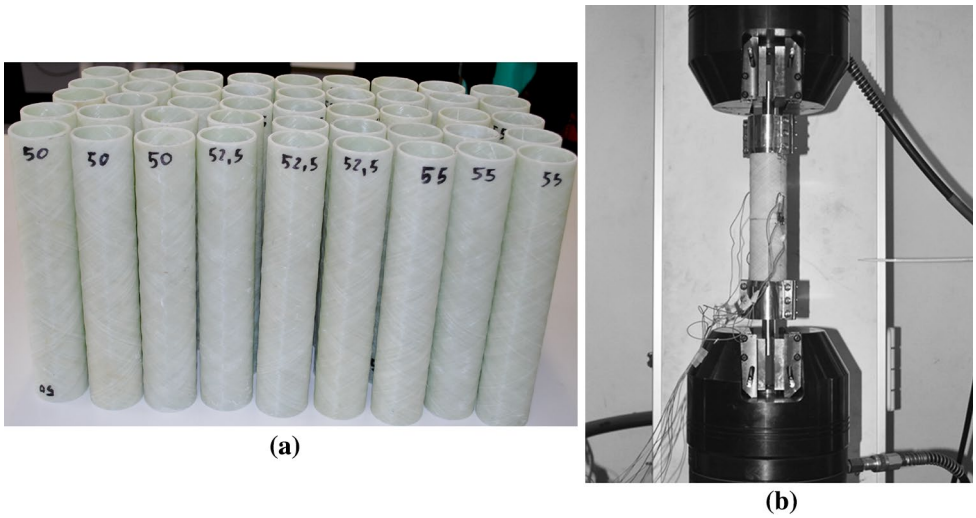

Fig. 5 **a** Total population of specimens. **b** General testing setup

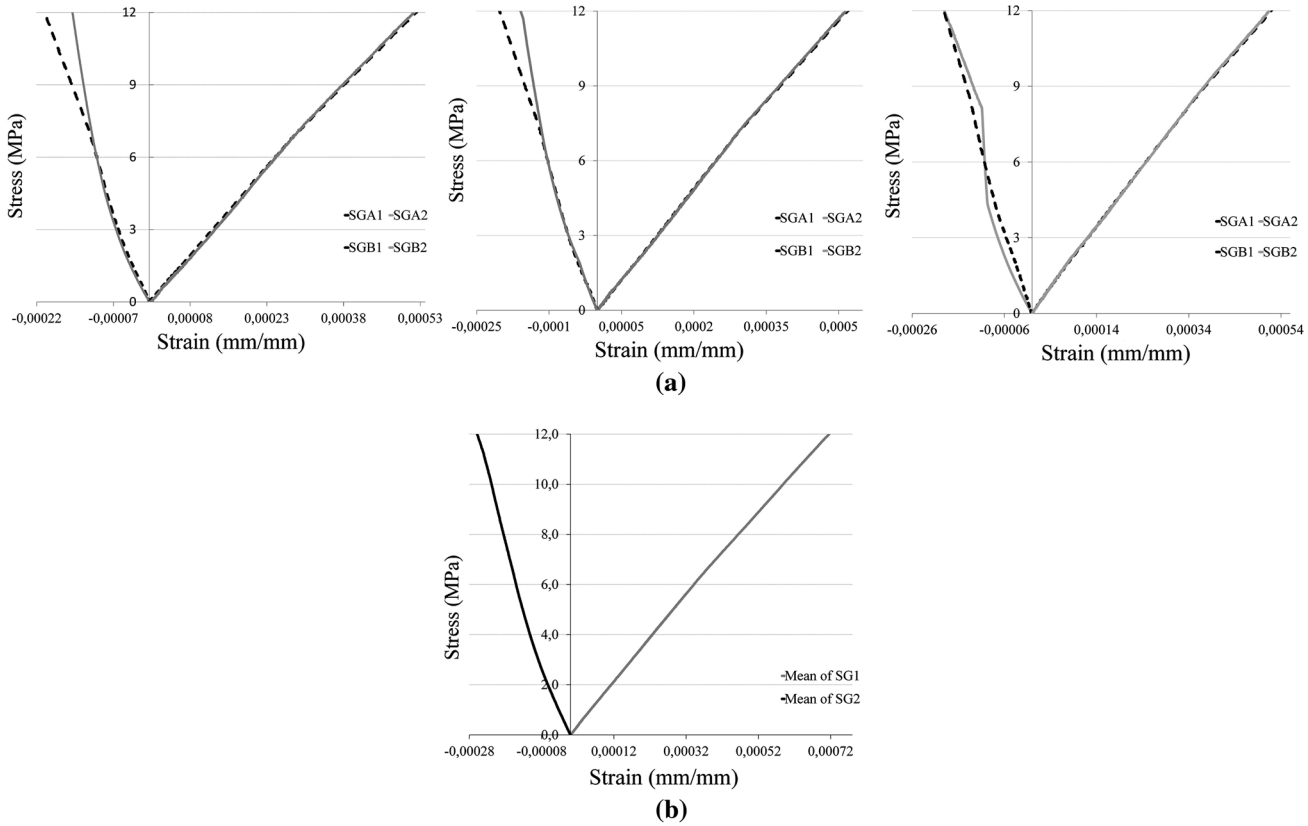

Fig. 6 **a** Stress–strain curve for each specimen. **b** Mean for all SPs ±50º

the fiber volume fraction V_{fr} was obtained experimentally [37]. Next, V_{fr} was input into the mRM to calculate the modulus in direction 1, E_{11}, the modulus in direction 2, E_{22}, the shear modulus in plane 1–2 G_{12}, and the Poisson's ratio in plane 1–2 ν_{12}, shown in Table 4. Finally, the theoretical design stress (S_d) and strain (ε) of the specimens were determined through CLT, as shown in Table 5.

3.3 CAD and simulation procedures

The literature has demonstrated that convergent results can be reached by modeling the raw materials separately and assembling them into a single complex model that includes the interactions among these sub-models [38]. Hence, this approach was used to create a virtual model for export to the FEA tool [39] to perform the simulation with the same boundary conditions as used in the experiments.

The parametric assembly was developed through SOLIDWORKS® [40], as shown in Fig. 2a–d. Here, a parallelogram cross section envelope was used to account for the hexagonal distribution of the dry filaments forming one composite roving-epoxy bundle.

The average roughness of the fiber filaments is 3.02 e^{-3} mm [41–43]; in this work, this value was multiplied by three to estimate the mean roughness of the filaments, corresponding to a 9.1 e^{-3} mm gap between each filament (Fig. 2d).

The interface thickness between two overlapping layers was taken as 9.0 e^{-2} mm, which was calculated as a function of the fiber volume fraction (55 %). This geometric distribution resulted in a bandwidth of 23.34 mm, which is very close to the actual bandwidth of 23.4 mm used in the specimen production.

This process was based on the equivalent fiber volume fraction (V_{fre}) for a bundle of unitary length given by Eq. 2. This model was developed by other researchers in a partially concluded study.

$$V_{\text{fre}} = \frac{\sum_{k=1}^{n} D_{fk}}{\sum_{k=1}^{n} S_e} \tag{2}$$

where D_{fk} = diameter of the kth fiber filament, with $D > 0$, S_e = envelope area of the polymer under consideration, with $S_e \geq D_{fk} \times 0.85$.

The mechanical and physical properties of each constituent material, i.e., the fiber strands and polymer, were input individually into the simulation tool [39], and the envelope

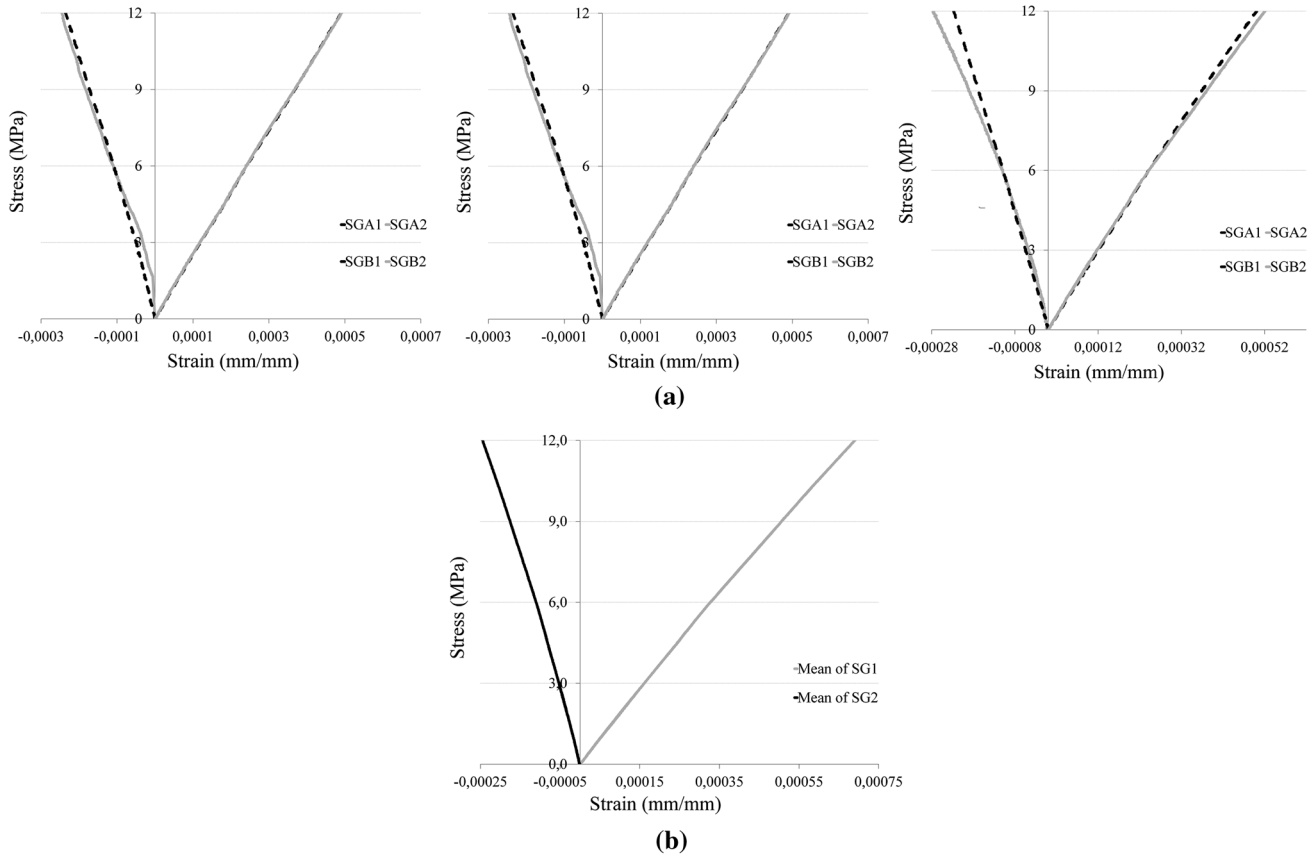

Fig. 7 **a** Stress–strain curve for each specimen. **b** Mean for all SPs of ±52.5°

area was selected as a function of V_{fre} using the geometrically calculated distances between each filament and the edges of the surrounding envelopes.

First, it was assumed that all the filaments were homogeneous, perfectly aligned relative to the winding machine axis, and perfectly hexagonally spaced. Next, the filamentary cross-sectional area needed to fill 55 % of a circumscribed rectangle was calculated via an iterative process. Here, the distance between the filaments was modified to achieve the cross-sectional area needed by the polymer to satisfy the relationship $V_{fre} + V_{pr} = 1$, where V_{pr} is the polymer volume fraction.

A detailed view of the cross section of the computer-aided drafting (CAD) model proposed with the polymeric film passing through the strands is shown in Fig. 3a and b.

The FEA tool considered the direction in which ε_1 was most positive as the major strain and the direction in which ε_3 was most negative as the minor strain. Therefore, the output in terms of the strain intensity is given as

$$\varepsilon_I = \max(|\varepsilon_1 - \varepsilon_2|, |\varepsilon_2 - \varepsilon_3|, |\varepsilon_3 - \varepsilon_1|) \tag{3}$$

where ε_I = maximum absolute value of strain intensity achieved.

The Lagrangian method was used to describe the friction and adhesion between the faces in contact within the materials as well as to predict the loss of adhesion between the contacting faces [41]. This method is based on the theory of Coulomb, which establishes that the maximum limit of friction should be less than or equal to the shear stress between the surfaces in contact.

The selected approach for the application of the forces between the faces in contact is described by Eq. 4, which addresses the problem of tangential contact friction between two faces.

$$\mathrm{d}\tau_I = t_i\left(\mu + P\frac{\partial\mu}{\partial P}\right)\mathrm{d}P + \left(\delta_{ij} - t_i t_j\right)\frac{\tau_{\lim}}{\left\|u^{\mathrm{pred}}\right\|}\mathrm{d}u_j + t_i t_j \frac{P}{\Delta t}\frac{\partial\mu}{\partial\|\dot{u}\|}\mathrm{d}u_j \tag{4}$$

where $\left\|u^{\mathrm{pred}}\right\|$ is the equivalent slip, which can be predicted for any given sub-step during the iteration process [42], and $\dot{u}$ is equivalent slip rate at a specific iteration number. Additionally, $t_{i,j}$ is the unitary vector in the slip direction, P is the contact normal pressure, μ is the friction coefficient calculated as $\tau_i = \mu_i P + b(i = 1{,}2)$, τ is the shear stress, and δ_{ij} is the displacement due to the shear effect with respect to the plane under consideration.

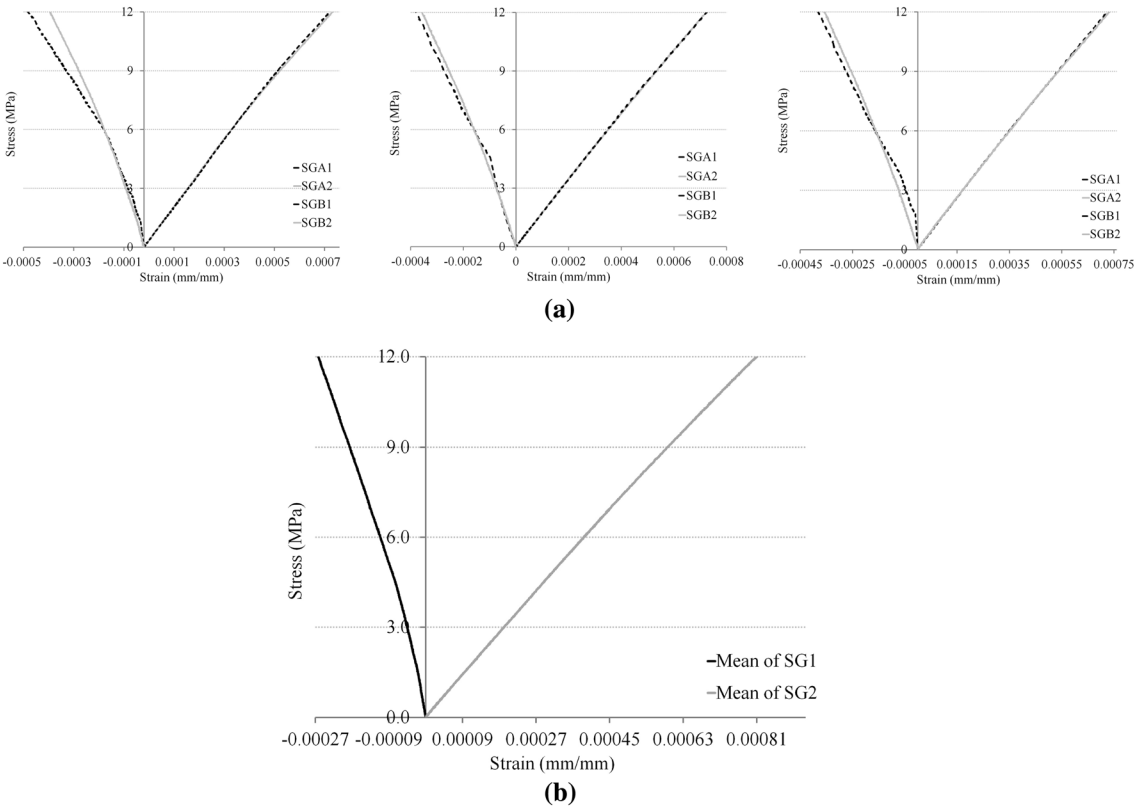

Fig. 8 a Stress–strain curve for each specimen. **b** Mean for all SPs ±55°

Table 7 Mechanical properties found by testing the three winding angles

Parameter	σ_A^a (MPa)	$\sigma_{T\vartheta}^a$ (MPa)	δ_A (mm)	*SG1A* (0º)	*SG1B* (90º)	*SG2A* (0º)	*SG2* (90º)
±50° - a	5.991	3.607	0.050309	0.000281	0.000280	−0.000114	−0.000113
±50° - b	6.002		0.050053	0.000282	0.000282	−0.000115	−0.000113
±50° - c	6.007		0.051517	0.000282	0.000284	−0.000117	−0.000115
Average	6.000		–	–	–	–	–
P	3435.11 (N)						
P_θ^b	2208.41 (N)						
S_{50}	572.535 (sq mm)						
S_{Lb}^c	612.198 (sq mm)						
E_{11}	21.30 (GPa)						
E_{22}	31.50 (GPa)						
G_{12}	7.57 (GPa)						
ε_{12}	0.000282						
ε_{21}	−0.000115						
ν_{12}	0.407						
ν_{21}	0.275						
±52.5°- a	5.998	3.927	0.051272	0.000290	0.000294	−0.000113	−0.000113
±52.5°- b	5.994		0.051755	0.000291	0.000290	−0.000112	−0.000115
±52.5°- c	5.996		0.053628	0.000293	0.000291	−0.000110	−0.000113
Average	*5.996*		–	–	–	–	–
P	3435.11 (N)						
P_θ^b	2198.60 (N)						
$S_{52.5}$	570.446 (sq mm)						
S_{Lb}^c	559.846 (sq mm)						
E_{11}	20.56 (GPa)						
E_{22}	34.92 (GPa)						
G_{12}	7.42 (GPa)						
ε_{12}	0.000292 (mm/mm)						
ε_{21}	−0.000112 (mm/mm)						
ν_{12}	0.386						
ν_{21}	0.227						
±55°- a	5.996	4.228	0.057472	0.000309	0.000305	−0.000105	−0.000114
±55°- b	6.000		0.054392	0.000307	0.000304	−0.000105	−0.000113
±55°- c	5.996		0.053437	0.000302	0.000306	−0.000107	−0.000112
Average	*5.997*		–	–	–	–	–
P	3435.11 (N)						
P_θ^b	2160.17 (N)						
S_{55}	560.376 (sq mm)						
S_{Lb}^c	510.874 (sq mm)						
E_{11}	19.64 (GPa)						
E_{22}	38.70 (GPa)						
G_{12}	7.23 (GPa)						
ε_{12}	0.000305						
ε_{21}	−0.000109						
ν_{12}	0.358						
ν_{21}	0.182						

[a] Stress calculated according to Eq. 1, as indicated in Fig. 9

[b] $P_{\vartheta A}$ = Decomposed loading according to the winding angle indicated in Fig. 9

[c] S_{Lb} longitudinal bundle area based on a one-half path of all strands in direction ± x degrees, for each winding angle and each considered wall thickness, P axial loading, S cross-sectional area of pipe, E_{11} elastic modulus in direction 1, E_{22} elastic modulus in direction 2, G_{12} shear modulus in plane 1-2, σ_A axial tensile stress, $\sigma_{T\vartheta}$ transversely resultant stress by winding angle, δ_A axial elongation, ε_{12} strain in plane 1–2, ε_{21} strain in plane 2–1, ε_{12} Poisson's coefficient in plane 1–2, ε_{21} Poisson's coefficient in plane 2–1

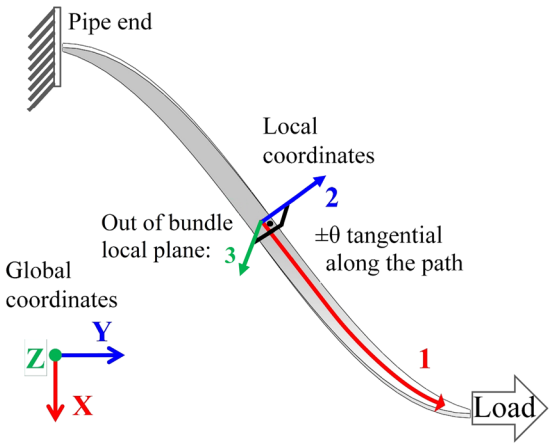

Fig. 9 Geometry used to calculate the normal loading of the bundles, by winding angle

Other models can also be used in simulation tools, such as those created through mathematical models; however, these models are often restricted to two dimensions (2D) by hardware limitations [43–48].

Table 6 shows the initial values of the mechanical and physical parameters input into the library of the FEA tool. After inputting these values, the mesh for each material was created, limiting the larger edge of the elements to no more than 1.8 mm.

It should be observed that the longitudinal cross-sectional area of the bundles forming the thickness of pipes, S_{Lb}, and the decomposed loading, P_θ refer to the local coordinates as shown in Fig. 7, rather than axial loading, P, and the cross-sectional area S.

Figure 4a and b shows the mesh for the specimen laminated with an angular variation of ±50°, and (c) shows the notation used by both CAD and FEA, with two strands hidden for internal visualization.

3.4 Experimental procedure

The tensile tests were performed in a servo-hydraulic universal testing machine (MTS®, model 810) with a 500-kN load cell using computational strain evaluation and displacement control.

Three specimens were randomly sampled from the 45 fabricated samples and conditioned in an environment with

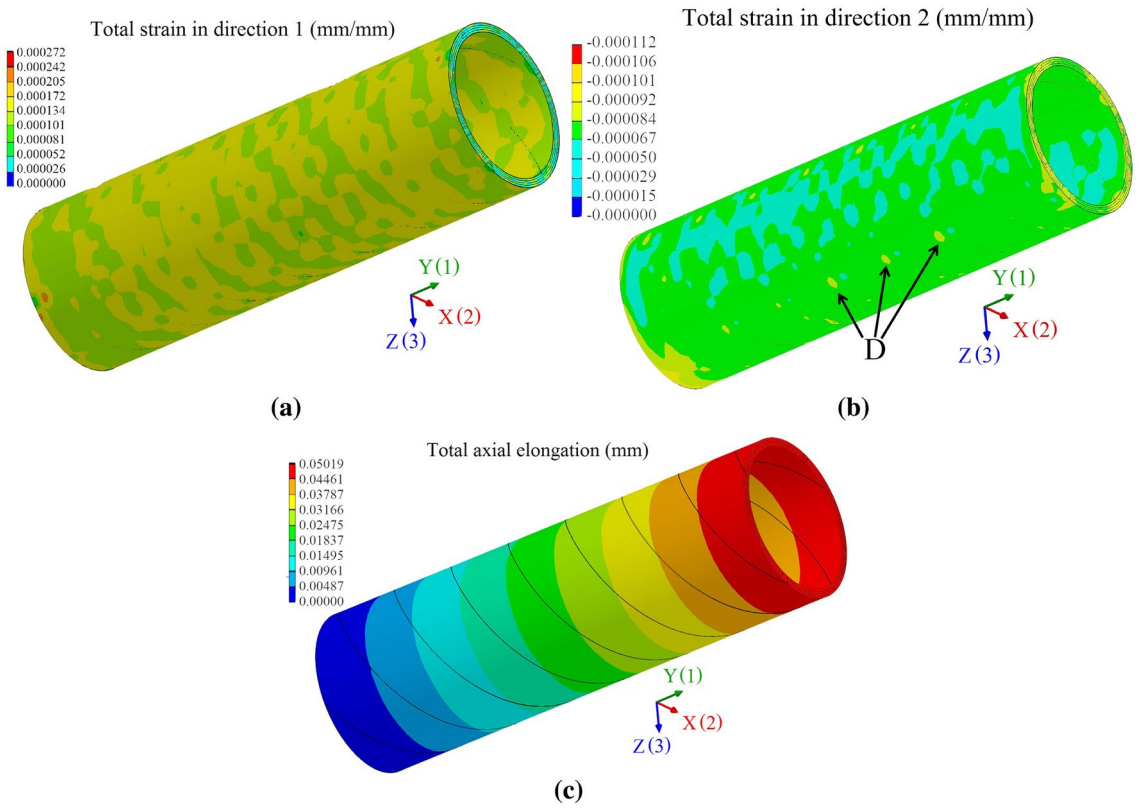

Fig. 10 **a** Strain in direction 1. **b** Strain in direction 2. **c** Total elongation (±50°)

controlled temperature and relative humidity. After 48 h, the specimens were equipped with a pair of axial–radial strain gages: the first placed in each pipe at the zero-degree circumferential mark and the second phased 180° from the first. Next, the specimens were monotonically loaded at a displacement velocity of 0.0106 mm s^{-1} until reaching 6 MPa or 12 MPa, as shown in Fig. 5a and b, respectively.

The elastic properties were determined from the 6 MPa loading for each specimen, and plots of the average stress versus recorded strain (Figs. 6, 7, 8a, b) were used to calculate the other elastic properties (Table 7).

Equation 5 was used to decompose the global stress (*Y*-axis) into the local axial and tangential loadings along each infinitesimal angle over the turned θ degree path. In this calculation, one-half turn of a helical model, with a known winding angle θ (Fig. 9), was considered for each roving bundle wound over the mandrel, according to Eq. 1 above.

$$\sigma_{T\theta} = \frac{\sigma_A w_b \tan\theta}{2D_{\text{avg}}} \tag{5}$$

where $\sigma_{T\vartheta}$ = resultant transversely stress for specific winding angle, σ_A = axial stress, considering the *Y*-axis as the axial direction for CAD and FEA, w_b = bundle width, θ = angle that the element or laminate makes with the axial direction, $D_{\text{avg}} = D_e - \frac{1}{2}t_\theta$, where t_θ is the wall thickness of each winding angle.

As the torsional moments were acting along the turned path, the Bernoulli–Navier principle was abandoned, and it was assumed that a flexural–torsional effect acted on the cross section.

4 Results and discussion

The fibers subjected to tensile stress had a strong tendency to straighten, especially with large displacements, inducing rotational moments around the local *X*-axis, i.e., transverse to the winding path. Because the *X*-axis passes through the wall in the direction tangential to the winding path, when the interlacing prevents the layers from moving (Fig. 9), localized failure occurs once the limit of rupture is reached. The failure then propagates throughout the laminate, leading to the collapse of the bundle interfaces.

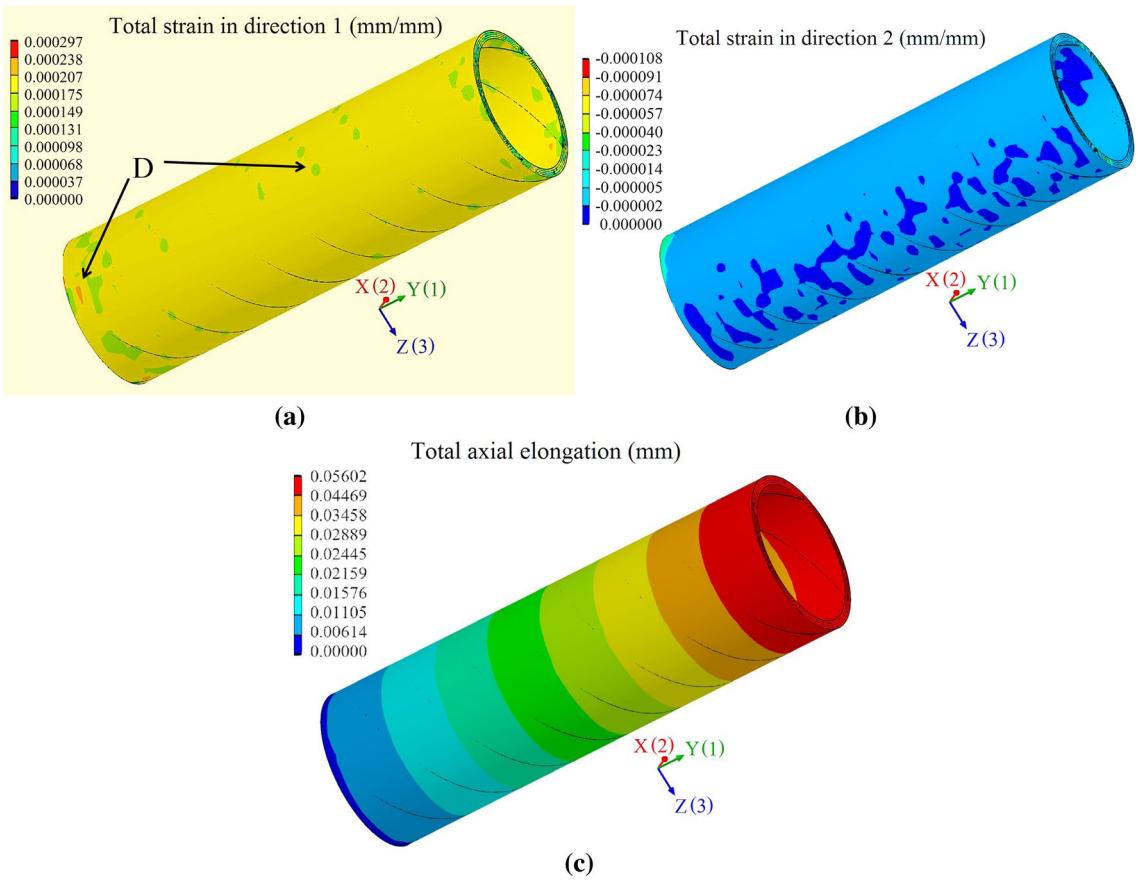

Fig. 11 **a** Strain in direction 1. **b** Strain in direction 2. **c** Total elongation (±52.5°)

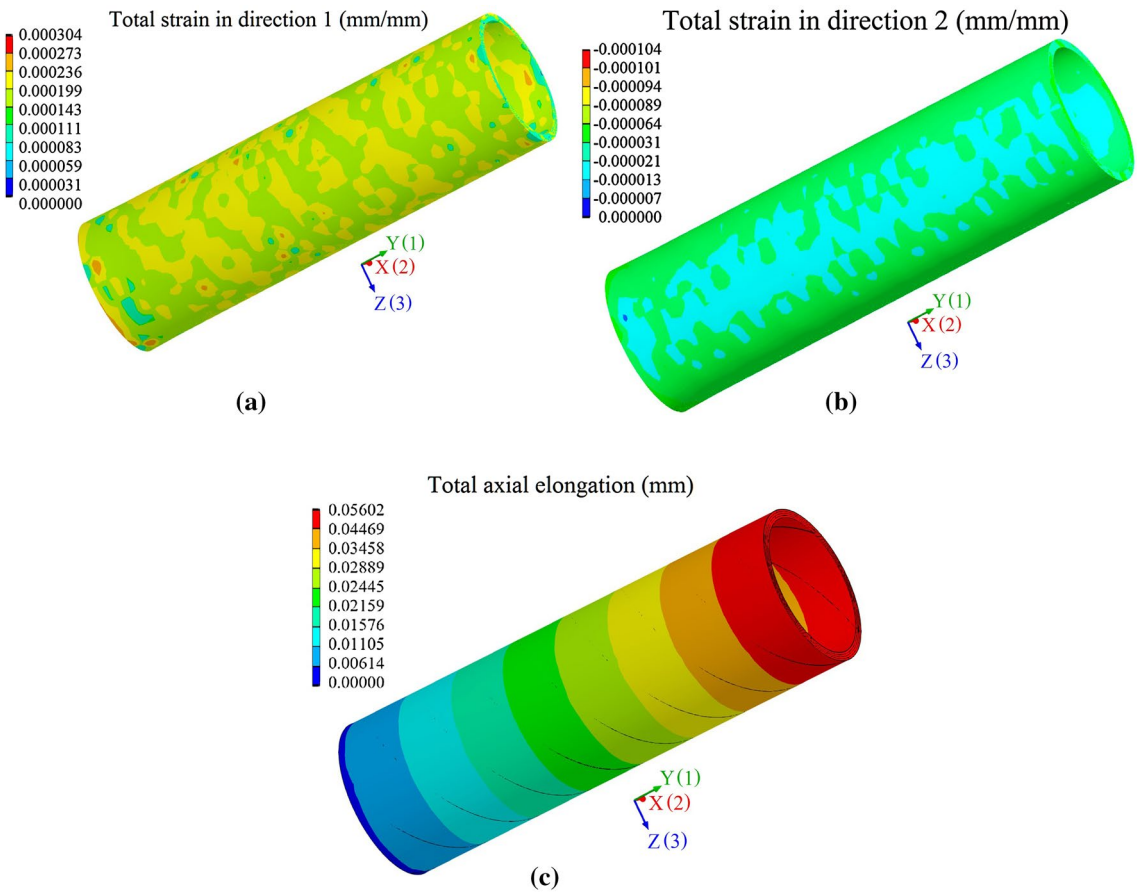

Fig. 12 **a** Strain in direction 1. **b** Strain in direction 2. **c** Total elongation (±55°)

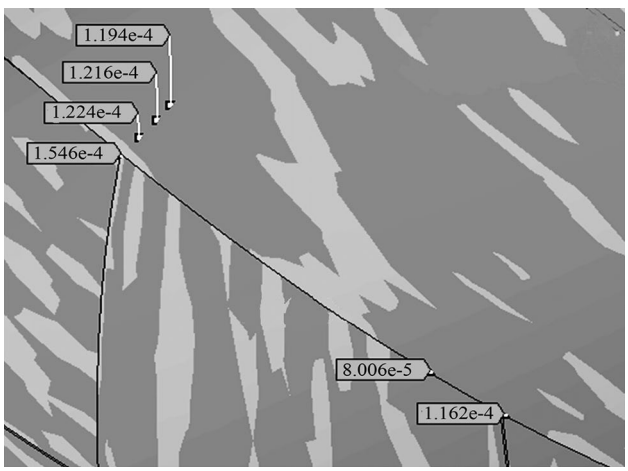

Fig. 13 Strains in overlapping points between two consecutive bundles due to axial loading

The simulation results were closest to the experimental results, whereas the theoretical results were very different from either of these sets of results, as we will see later. The theoretical results differed substantially from the simulation results because the former treated the material as a perfectly bonded whole, while the latter treated it as a set of individually stacked layers.

Although the limit values were similar to the experimental results, the strains in plane 2–1 were inhomogeneous, with larger variations in the intermediate loading level.

The simulated models reveal a spreading of the strains, which formed niches along the pipes, with some points of high strain localized along the pipe length, as shown in Figs. 10, 11, and 12a–c. This behavior was observed throughout the laminate, which may indicate that the stretching and movement restrictions caused localized displacements and concentration of stress, especially in intersections between layers as indicated in same figures by capital letter 'D'. Other indications in the same direction are the strains due to axial loading been occurred in simulation, where two consecutive bundles presented jumps in the strain level, when they were near from overlapping region, as shown in Fig. 13.

The quasi-linear behavior of the experimental results was verified through the plotted stress–strain curves. In contrast, according to the FEA, quasi-linear behavior

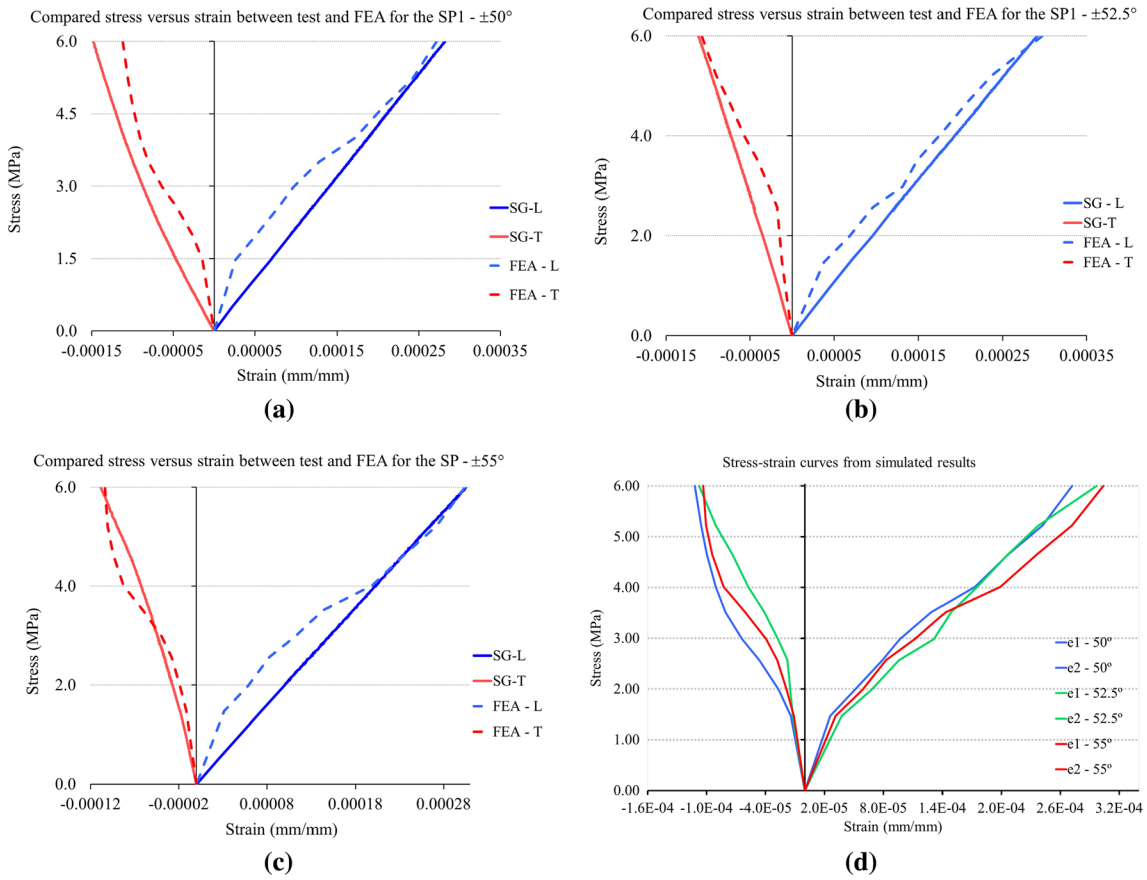

Fig. 14 **a** Strains from FEA and tests for ±50°. **b** Strains from FEA and tests for ±52.5°. **c** Strains from FEA and tests for ±55°. **d** Strains from FEA for each angular variation

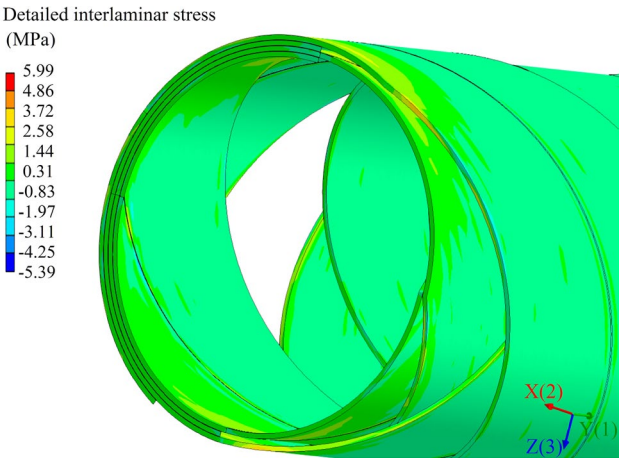

Fig. 15 Interlaminar stress effects (traction and compression) on the layers

only occurred around 1.6 MPa, above which the behavior became non-linear, as seen in Fig. 14a–d.

As the filaments are stretched by traction, they are progressively compressed laterally. This behavior can be explained by the load level difference between experiments, which achieved 12.5 % of the average ultimate limit stress of pipes. Therefore, there were innumerous points at which the strands interacted with one another, and the resulting internal stresses changed from traction to compression. In Fig. 15, some of the strands are hidden to visualize the inner layers and the concentration of stress on the strand edges.

The moduli E_{11}, E_{22}, and G_{12} and the strains ε_{12} and ε_{21} obtained via mRM versus CLT and experimentally (Tests) versus FEA were compared for each winding angle as shown in Figs. 16, 17, 18 and 19a and b.

The plot of the strains for mRM and CLT is not presented herein because the parameters were theoretical

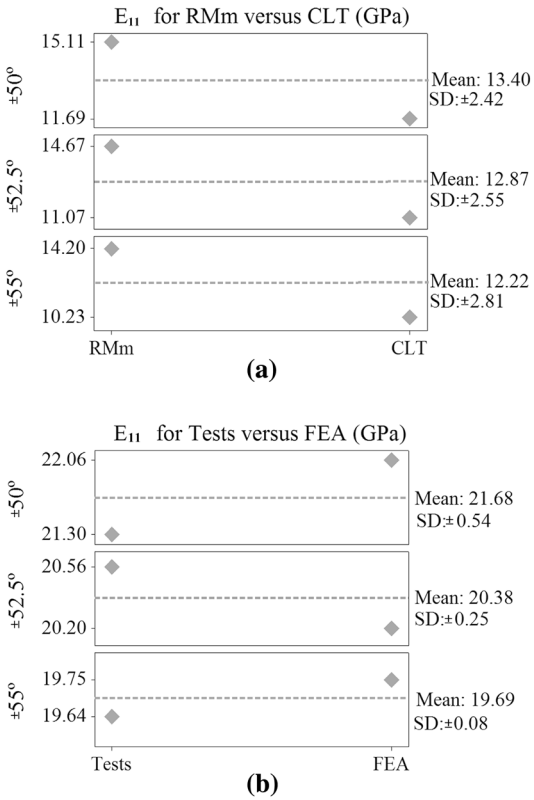

Fig. 16 **a** Compared values of E_{11} for RMm versus CLT, and **b** Tests versus FEA, for all typologies with the mean and the SD

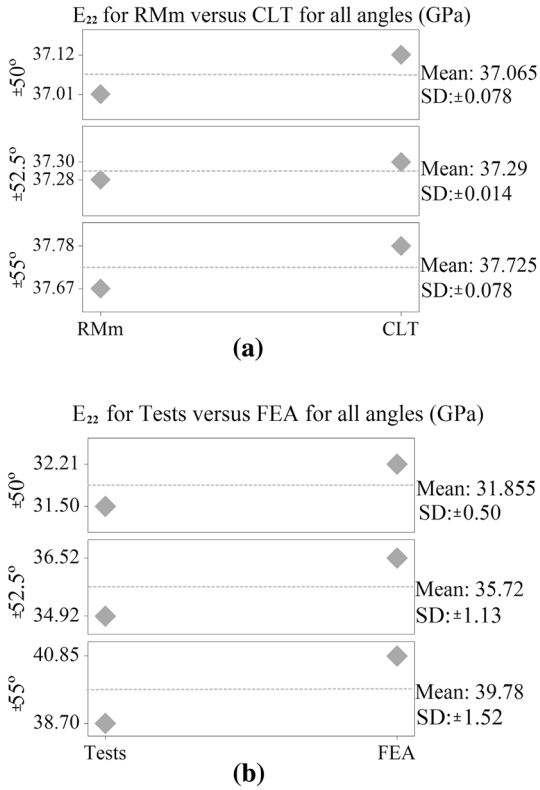

Fig. 17 **a** Compared values of E_{22} for RMm versus CLT, and **b** Tests versus FEA, for all typologies with the mean and the SD

values obtained from the literature and then averaged. The mRM and CLT provided higher strain values than the Tests and FEA (Table 8).

For the pair mRM–CLT, the largest standard deviation—SD for the modulus E_{11} was found for the angular variation of ±55°, for which the mean value was ±2.81 GPa. Meanwhile, for the pair Tests–FEA, the SD for E_{11} was highest for the angular variation of ±50°, for which the mean value was ±0.54 GPa. In the first case, the SD was 20 % higher than the average, while in the second case, the SD was 2.5 % less than the average.

For E_{22}, the highest variation occurred for the pair Tests–FEA and an angular variation of ±55°; the value, ±1.52 GPa, corresponded to a 3.8 % deviation from the average. In contrast, the pair mRM–CLT presented the lowest SD of all moduli, with a value of ±0.014°GPa for the angular variation of ±52.5°.

Among the results obtained, the highest convergence was obtained for the G_{12} modulus for the pair Tests–FEA, with an SD of zero for the angular variation ±52.5°. Meanwhile, the most divergent was the E_{11} of the ±55° for the pair mRM–CLT (Figs. 15, 16).

Regarding the strains, the SDs were all lower than 1.0 mm/mm^{-5}. The highest SD (±7.1 mm/mm^{-6}) was obtained for ε_{12} from the typologies ±50° and ±55°, while the lowest (±2.1 mm/mm^{-6}) was obtained for ε_{21} from the typology ±50°.

The results of these various analyses were somewhat consistent regarding the angular variation but did not follow a regular pattern, as seen in Figs. 18 and 19.

5 Conclusions and remarks

In the analysis of filament wound elements, the standards [49, 50] are unlikely to provide accurate results. This is because the recommended directions are not coincident with the winding angles: there is missing information regarding the actual strain in the direction of the bundles. To address this problem, other analyses can be used to determine this correlation experimentally rather than theoretically. In this work, experimental, simulation, and theoretical analysis techniques were compared in the context of automated filament winding lamination.

The results showed that the results obtained from the theoretical models, computational simulation, and experimental analysis of this type of structure varied slightly.

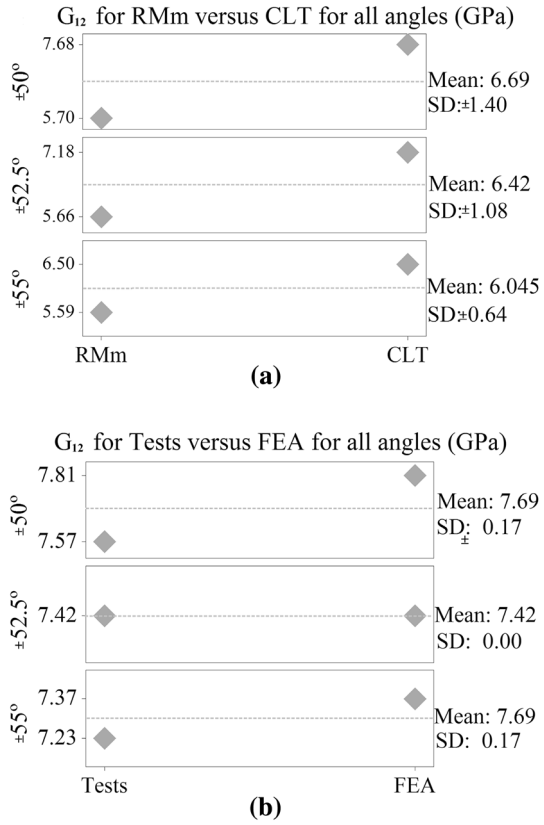

Fig. 18 **a** Compared values of G_{12} for RMm versus CLT, and **b** Tests versus FEA, for all typologies with the mean and the SD

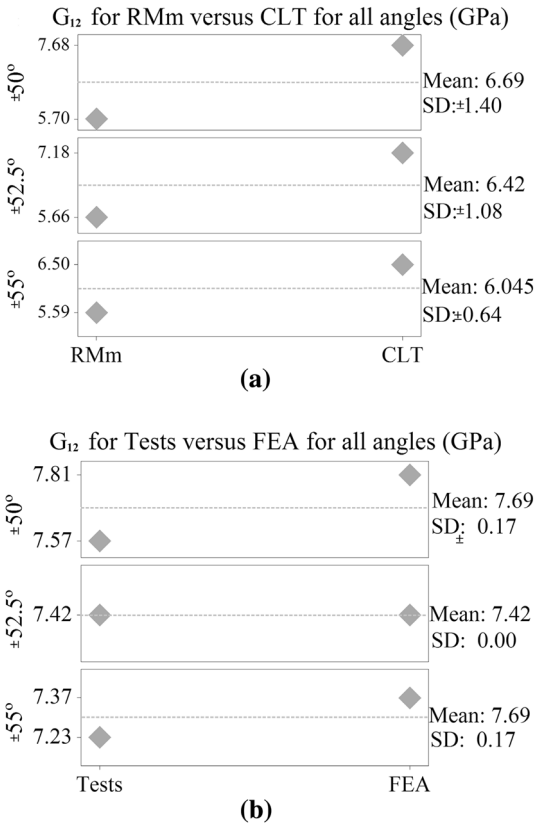

Fig. 19 **a** Values of ε_{12} for Tests versus FEA, for all typologies with the mean and the SD. **b** Values of ε_{21} for Tests versus FEA, for all typologies with the mean and the SD

The analyses based on the mRM and CLT, which consider perfectly adhered laminates, use the Kirchhoff hypothesis wherein the fibers normal to the middle plane of the laminate remain normal during the deformation and retain their initial length. Under transverse strain, the plate deflections are significantly smaller than the thickness of the plate under consideration [51], which implies that

$$e_{xz} = e_{yz} = e_z = 0 \quad \text{and} \quad s_{xz}, s_{yz}, s_z << s_{xy}, s_y, s_x.$$

The boundary conditions of each theoretical analysis may have contributed to the difference between the pair of theoretical results with respect to the results of the tests and FEA. Moreover, the most meaningful observation was the convergence and greatest similarity between the results of the tests and the FEA regarding the G_{12} modulus, whereas the greatest variation occurred for the pair mRM–CLT for the E_{11}.

The variations of the moduli and respective Poisson ratios followed the expected behavior: the distance between the values increased as the winding angle changed when the laminates were rotated in direction 2 (x in this work).

In turn, the experimental analysis conducted based on the strain gage positioning standards may not be the best suited for curved surfaces produced by filament winding.

The moduli values followed a pattern for most of the winding angles and analysis methods; however, additional testing is required to confirm whether this pattern is real. All the other results are summarized for each analysis method and angular variation and revealed the same trends as described for the moduli [52].

Additional tests should be performed with a larger number of strain gages, some aligned along the path of the strands and others perpendicular to this path. In both this study and the literature, significant differences were found between the results of tensile (or compressive) tests for 180- and 600-mm-long specimens [1, 24, 52].

Software packages exist for specific application to composites; however, they are still too expensive for use by small- and medium-sized companies in emerging countries [53].

Finally, similar analyses should be performed using other winding angles to validate the approach for the filament winding fabrication and integrated CAD.

Table 8 A comparison of the mechanical properties obtained through all analyses

Analysis type	Parameter	Winding angle		
		±50º	±52.5º	±55º
Tests	E_{11} (GPa)	21.30	20.56	19.64
	E_{22} (GPa)	31.50	34.92	38.70
	G_{12} (GPa)	7.57	7.42	7.23
	ε_{12} (mm/mm)	0.000282	0.000292	0.000305
	ε_{21} (mm/mm)	−0.000115	−0.000112	−0.000109
	ν_{12}	0.407	0.386	0.358
	ν_{21}	0.275	0.227	0.182
CLT	E_{11} (GPa)	11.69	11.07	10.23
	E_{22} (GPa)	37.12	37.30	37.78
	G_{12} (GPa)	7.68	7.18	6.50
	ε_{12} (mm/mm)	0.000397	0.000411	0.000432
	ε_{21} (mm/mm)	−0.000125	−0.000122	−0.000117
	ν_{12}	0.315	0.297	0.271
	ν_{21}	0.10	0.09	0.07
mRM	E_{11} (GPa)	15.11	14.67	14.20
	E_{22} (GPa)	37.01	37.28	37.67
	G_{12} (GPa)	5.70	5.66	5.59
	ε_{12} (mm/mm)	0.000397	0.000411	0.000432
	ε_{21} (mm/mm)	−0.000125	−0.000122	−0.000117
	ν_{12}	0.315	0.297	0.271
	ν_{21}	0.129	0.117	0.102
FEA	E_{11} (GPa)	22.06	20.20	19.75
	E_{22} (GPa)	32.21	36.52	40.85
	G_{12} (GPa)	7.81	7.42	7.37
	ε_{12} (mm/mm)	0.000272	0.000297	0.000304
	ε_{21} (mm/mm)	−0.000112	−0.000108	−0.000104
	ν_{12}	0.412	0.362	0.341
	ν_{21}	0.170	0.131	0.116

This research was supported by the "Brazilian Federal Agency for the Support and Evaluation of Graduate Education (CAPES)" of the Ministry of Education of Brazil.

References

1. Ortenzi A, De Carvalho J, Corvi A (2012) Comparison behavior for GFRP filament wound pipes with two different sectional areas regarding high temperature. In: OMAE conference on ocean, offshore, and artic engineering (ed ASME), Rio de Janeiro, Brazil, paper no. OMAE2012-84256. ASME, New York, pp 955–961
2. Ortenzi A, Corvi A, Virga A (2014) Preliminary study on the acoustic emission wave velocity on filament wound glass fiber reinforced polymer pipes and its correspondence with the winding angle. Adv Mater Res 891–892:1243–1248
3. Chun-Gon K et al (2002) Optimal design of filament wound structures under internal pressure based on the semi-geodesic path algorithm. Compos Struc 67:443–452
4. Vaughan DJ (1998) Laminate design. In: Peters ST (ed) Handbook of composites, 2nd edn. Chapman & Hall, Mountain View, pp 686–708
5. Quinn JA (2002) Composites design manual. 3rd (ed), Ch. 1-4. James Quinn Associates Ltd, Liverpool
6. Piggott M (2002) Load bearing fibre composites. 2nd (ed). Kluwer Academic Publishers, Toronto, pp 20–50, 95–123
7. Daniel IM, Ishai O (1994) Engineering mechanics of composite materials. Oxford University Press, New York, pp 89–112
8. Hyer MW (1998) Stress analysis of fiber-reinforced composite materials. WCB McGraw-Hill, Virginia, pp 98–138
9. Vasiliev VV, Morozov EV (2001) Mechanics and analysis of composite materials. ELSEVIER, Natal, pp 41–62, 102–134
10. Hoa SV, YU CW, Sankar TS (1985) Analysis of Filament Wound Vessel Using Finite Elements. J Compos Struc 3:1–18
11. Hinton MJ, Soden PD (1998) Failure of ±55° filament wound glass/epoxy composite tubes under biaxial compression. J Compos Mater 32:1618–1647
12. Kaddour AS, Hinton MJ, Soden PD (2002) A comparison of the predictive capabilities of current theories of composite laminates judged against experimental evidence. Compos Sci Technol 62:1725–1797
13. Rotem A (1998) Prediction of laminate failure with the Rotem failure criterion. Compos Sci Technol 58(7):1083–1094
14. Tsai SW, Hoa SV and Gay D (2002) Composite materials—design and applications. CRC Press, New York, pp 23–52, 210–258
15. Zinoviev PA et al (1997) The strength of multilayered composites under a plane stress state. J Compos Sci Technol 58:1209–1223
16. Hart-Smith LJ (2002) Comparison between theories and test data concerning the strength of various fiber–polymer composites. J Compos Sci Technol 62:1591–1618
17. Puck A, Schürman H (1996) Failure analysis of frp laminates by means of physically based phenomenological models. J Compos Sci Technol 58:1045–1067
18. Tsai SW, Wu EM (1971) A general theory of strength for anisotropic materials. J Compos Mater 5:58–80
19. Hashin Z (1983) Analysis of composites materials. J Appl Mech 50:481–485
20. Rousseau J, Perreux D, Verdière N (1999) The influence of winding patterns on the damage behavior of filament-wound pipes. Compos Sci Technol 59:1439–1449
21. Meijer G, Ellyin F (2008) A failure envelope for ±60° filament wound glass fiber reinforced epoxy tubular. Compos A 65:555–564
22. Ellyin F (1874) Maser R (2004) Environmental effects on the mechanical properties of glass-fiber epoxy composite tubular specimens. Compos Sci Technol 64:1863
23. Kaddour AS, Soden PD, Hinton MJ (2003) Behaviour of ±45° glass/epoxy filament wound composite tubes under quasi-static Composite Tubes under biaxial tension–compression loading: experimental results. Compos B 34:689–704
24. Ortenzi A, Tarpani JR, De Carvalho J (2010) Compared behavior of filament wound pipes tested at room temperature and high temperature. In: SEICO—SAMPE international conference (ed Erath MA), Paris, France, SEICO, Paris, pp 584–589
25. Hu G et al (1998) Mechanical behavior of ∞55º filament-wound glass-fibre/epoxy-resin tubes—III. Macromechanical model of the macroscopic behavior of tubular structures with damage and failure envelope prediction. Compos Sci Technol 58:19–29
26. Abel-H F (2005) Filament winding of revolution structures. J Reinf Plast Compos 24:855–868
27. Polini W, Sorrentino L (2006) Winding trajectory and winding time in robotized filament winding of asymmetric shape parts. J Compos Mater 39:1391–1410

28. Koussios S, Bergsma OK (2006) Friction experiments for filament winding applications. J Thermoplast Compos Mater 19:5–34
29. Meink TE, Huybrechts S, Shen M-HH (2002) Processing induced warpage of filament winding composite cylindrical shells. J Compos Mater 36:1025–1047
30. Binienda WK, Wang Y (1999) Stresses reduction in filament wound composite tubes. J Reinf Plast Compos 18:684–701
31. Kabir MZ (2000) Finite element analysis of composite pressure vessels with a load sharing metallic liner. Compos Struct 49:247–255
32. Arif AFM, Malik MH, Omari AS (2014) Impact resistance of filament wound pipes: a parametric study In: ASME 2014 Pressure vessels and piping conference. (ed ASME), Anahein, USA, ASME, New York, pp not available
33. Zhou C, Xia Z, Yong Q (2006) Micro mechanical model of filament wound composite pipes with damage analysis. In: ASME 2006 pressure vessels and piping/ICPVT-11 conference. (ed ASME), Vancouver, Canada, ASME, New York, pp 67–74
34. Chen MC, Clewlow LNO (1977) Computer analysis of filament reinforced metallic-spherical pressure vessels. Comput Struct 7:93–102
35. Du J et al (2011) Design and fabrication of the world's first filament wound section X class II vessels. In: ASME 2011 Pressure vessels and piping conference. (ed ASME), Baltimore, USA, ASME, New York, pp 59–68
36. Schlottermüller M et al (2003) Thermal residual stress simulation in thermoplastic filament winding process. J Thermoplast Compos Mater 16:497–518
37. ASTM D3171:2010 (2010) Standard test methods for constituent content of composite materials
38. Durville D (2007) Finite element simulation of textile materials at mesoscopic scale. In: Finite element modelling of textiles and textile composites, https://hal-ecp.archives-ouvertes.fr/hal-00274046. Accessed 18 Feb 2015
39. SAP IP Inc (2012) ANSYS Workbench V.13.0, User's guide. October 2012
40. DS. Solidworks 2013 (2013) Academic version manual. September 2013
41. Lukas D, Pan N (2003) Wetting of a fiber bundle in a fibrous structure. Polym Compos 24(3):314–322
42. Lukas D et al (2006) Morphological transitions of capillary rise in a bundle of two and three solid parallel cylinders. Phys A 371:226–248
43. Wang SK et al (2011) Comparison of wettability and capillary effect evaluated by different characterizing methods. In: 18th International conference on composite materials. Online access: http://www.iccm-central.org/Proceedings/ICCM18proceedings/data/2.%20Oral%20Presentation/Aug24%28Wednesday%29/W06%20Experimental%20Techniques/W6-3-IF0508.pdf
44. Alfano G, Crisfield MA (1990) Finite element interface models for the delamination anaylsis of laminated composites: mechanical and computational issues. Int J Numer Methods Eng 50:1701–1736
45. Benson DJ, Hallquist JO (1990) A single surface contact algorithm for the post-buckling analysis of shell structures. Comput Meth Appl Mech. Eng 78–2:141–163
46. Mathworks- Matlab-Simulink (2011) Academic version 2012 User's guide. September 2011
47. Alberty J et al (2002) Matlab implementation of the finite element method in elasticity. Computing 69:239–263
48. Voyadjis GZ, Kattan PI (2005) Mechanics of composite materials with MATLAB. Springer, Baton Rouge, pp 79–189
49. Kirchhoff GR (1874) Vorlesungen über analytische Mechanik mit Einschluss der Hydrodynamik und der Theorie der Elastizität fester Körper. TEUBNER, Liepzig, p 1874
50. Niklewicz J, Sims GD (2002) Size effects in composite materials. National physics Laboratory. NPL Report, MATC (A) 74, p 23
51. MSC-Digimat (2013) Instruction book—The multi-scaling material modeling platform. November 2013
52. ASTM: ASTM D2105—97 (Reapproved 2007). Standard test method for longitudinal tensile properties of "Fiberglass" (Glass-FiberReinforced Thermosetting-Resin) pipe and tube
53. American Petroleum Institute. API 15HR (2001). Specification for fiberglass Line Pipe.—Appendix F. 3rd Ed